Air bubbles in fibrous caseinate gels investigated by neutron refraction, X-ray tomography and refractive microscope

Tian, Bei; Wang, Zhaojun; van der Goot, Atze Jan; Bouwman, Wim

Publication date
2018

Document Version
Final published version

Published in
Food Hydrocolloids

Citation (APA)
Tian, B., Wang, Z., van der Goot, A. J., & Bouwman, W. (2018). Air bubbles in fibrous caseinate gels investigated by neutron refraction, X-ray tomography and refractive microscope. *Food Hydrocolloids*, *83*, 287-295.

Food Hydrocolloids 83 (2018) 287–295

Contents lists available at ScienceDirect

Food Hydrocolloids

journal homepage: www.elsevier.com/locate/foodhyd

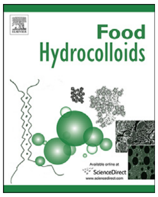

Air bubbles in fibrous caseinate gels investigated by neutron refraction, X-ray tomography and refractive microscope

Bei Tian [a], Zhaojun Wang [b], Atze Jan van der Goot [b], Wim G. Bouwman [a], *

[a] Department of Radiation Science and Technology, Faculty of Applied Science, Delft University of Technology, Mekelweg 15, 2629JB Delft, the Netherlands
[b] Food Process Engineering, Wageningen University, PO Box 17, 6700AA Wageningen, the Netherlands

A R T I C L E I N F O

Article history:
Received 29 January 2018
Received in revised form
4 May 2018
Accepted 5 May 2018
Available online 9 May 2018

Keywords:
Calcium caseinate
Neutron refraction
X-ray tomography
Meat analogue
Bubble morphology
Isotope effect

A B S T R A C T

Fibrous protein gels have the potential to form the basis for the next-generation of meat analogue. It is suggested that fibre anisotropy is related to air bubbles present in the gel. Given the complexity and heterogeneity of the samples, several quantitative techniques are needed to ensure a comprehensive understanding of the air bubbles. We performed neutron refraction experiments to study the size and shape of the air bubbles in three calcium caseinate samples containing different H_2O to D_2O ratios. Refractive microscopy and X-ray tomography (XRT) analysis were done on the same samples to provide complementary information. The deformation degree and average width of the air bubbles were obtained from both the XRT and neutron refraction experiment. A neutron refraction model calculates the average area and volume of a single air bubble, which correspond to the largest area and volume fractions of all the air bubbles from the XRT analysis. Additionally, we found that the H_2O to D_2O ratios in the sample largely influence the size, number distribution and deformation degree of the air bubbles. The neutron refraction technique can be a simple and complementary method to help understanding the role of air bubbles in the meat analogue.

1. Introduction

Many food products can be seen as composite materials whose textures are determined synergistically by the fillers (dispersed phase) and the matrix (continuous phase) (van Aken, Oliver, & Scholten, 2015; van der Sman, 2016). For example, the viscoelastic properties of a dough change after the inclusion of air (Dobraszczyk & Morgenstern, 2003); the hardness of a cheese increases with decreasing fat content (Bryant, Ustunol, & Steffe, 1995), and the rheological and sensory properties of a chocolate rely on the subtle balance between sugar, cocoa butter and cocoa powder (Afoakwa, Paterson, & Fowler, 2007). Characterizing the microstructure of the dispersed phase is crucial to understanding the macroscopic properties of the food product. (see Fig. 7)

An interesting composite food material is a fibrous protein gel made of calcium caseinate (Grabowska, van der Goot, & Boom, 2012; Manski et al., 2007a). Since the fibrous structure resembles real meat, calcium caseinate is considered as a promising candidate for the next-generation meat analogue (Manski et al., 2007b). Air is the only dispersed phase in such a fibrous protein gel. It has always been present in different types of meat analogues (Krintiras, Diaz, Van der Goot, Stankiewicz, & Stefanidis, 2016; Manski et al., 2007c), but it was not until recent that its contribution to the fibres' mechanical properties was brought up (Dekkers, Hamoen, Boom, & van der Goot, 2018). The air bubbles are elongated along the shear rate direction and its maximum length corresponds to the highest anisotropy index of the fibres. This suggests that characterising the air bubbles can provide complementary information on the anisotropy of the fibres. However, not many techniques are available to characterize them.

X-ray computed tomography (XRT) is a common and non-destructive technique to study the size, shape and amount of air in composite materials (Das et al., 2016; Kuang, Ying, Ranieri, & Sansalone, 2015; van Dalen, Blonk, van Aalst, & Hendriks, 2003). The contrast in XRT comes from the absorption difference between the protein matrix and the air. XRT has been applied to demonstrate how gelatin peptide fortified the microstructure of frozen mousses against the freeze-thaw cycle (Duquenne et al., 2016), to evaluate the performance of different gluten (Bellido,

---

* Corresponding author.
E-mail addresses: b.tian-1@tudelft.nl (B. Tian), zhaojun.wang@wur.nl (Z. Wang), atzejan.vandergoot@wur.nl (A.J. van der Goot), w.g.bouwman@tudelft.nl (W.G. Bouwman).

https://doi.org/10.1016/j.foodhyd.2018.05.006

Scanlon, Page, & Hallgrimsson, 2006) or gluten-free dough recipes (Demirkesen et al., 2014), and to support a new preparation method for making a soy-protein based hydrogel (Dekkers et al., 2018; Guo et al., 2013). As powerful as XRT can be, a composite food system is inherently heterogeneous and complex (Donald, 2004), so no single remedy is sufficient to provide a complete view of the sample. The drawbacks of XRT are the large dataset, possible imaging artifacts, and the treatment of the raw data can be dependent on the operators (Cnudde & Boone, 2013; Maire & Withers, 2014; Schoeman, Williams, du Plessis, & Manley, 2016). To ensure a comprehensive and unbiased understanding of the sample, we need several quantitative approaches to characterize the air bubbles.

Neutron refraction is another suitable technique to study the air bubbles. It is performed by the Spin-Echo Small Angle Neutron Scattering (SESANS) instrument (Plomp, Barker, De Haan, Bouwman, & van Well, 2007). The SESANS instrument measures the change in neutron direction. This results in a decrease of the polarisation of neutron beam. When the size of an object is small (e.g., up to a few micrometers), the change in polarisation is contributed by the scattering of the object. The scattering depends on the dimension of the scattering particle, volume fraction and scattering length density contract. Thus, the size information is readily present in the measured depolarisation curve (Berk & Hardman-Rhyne, 1988; de Haan, Plomp, & van Well, 2007a). It was applied to quantify the microstructure of globular protein gels (Ersch et al., 2016), to explain the mechanical properties of cross-linked casein micelles (Nieuwland, Bouwman, Bennink, Silletti, & de Jongh, 2015), and to compare the gel structure between curdling and acidified milk (Tromp & Bouwman, 2007). When the size of an object is large (e.g., over tens of micrometers), neutrons passing through the object will be rather refracted than scattered (Berk & Hardman-Rhyne, 1988; de Haan, Plomp & van Well, 2007b). The amount of refraction depends on the geometry of the object instead of the size, so the size information is not directly visible in the detected signal. The neutron refractive index difference between the object and its surrounding matrix determines the contrast. Neutron refraction has been less explored than neutron scattering. To our knowledge, it has only been used in food-related research once, to characterize the number of layers in a fibrous structure made of soy protein isolate and gluten (Krintiras, Göbel, Bouwman, Van Der Goot, & Stefanidis, 2014). The fibre was approximated as infinitely long cylinders with a spread in orientation. However, the geometry of a fibre is very different from that of an elongated air bubble. As a result, another model is needed so that the information obtained from the neutron refraction technique is comparable to the others.

In this study, we demonstrated multiple techniques: neutron refraction combined with XRT and refractive microscope add more certainty to a comprehensive understanding of the air bubbles dispersed in the fibrous calcium caseinate gel. To show the sensitivity of the contrast, we prepared three samples using 100% H_2O, 50%v/v H_2O+50%v/v D_2O and 100% D_2O. An improved model based on the microscopy images was proposed to fit the neutron refraction data. Parameters such as deformation degree, average width and orientation of the air bubbles can be extracted from the model, which agrees with the XRT results.

2. Material and methods

2.1. Materials

Roller dried calcium caseinate powder was provided by DMV International, Veghel, The Netherlands. The calcium caseinate powder contains 90%*wt* protein and 1.2%*wt* calcium according to the manufacturer's specification. Heavy water (deuterium oxide, D_2O, $\rho = 1.107\text{g/mL}$) with 99.9% deuterium was used (Sigma-Aldrich, Canada).

2.2. Preparation of the structure

An in-house developed shear device with gap angle 2.5° (Wageningen University, The Netherlands) was used to obtain the anisotropic calcium caseinate samples. The shear device is depicted and described in detail in (Manski et al., 2007a; van der Zalm, Berghout, van der Goot, & Boom, 2012). A heating and a cooling water bath were connected to the rotating and stationary cone to control the temperature. Protein premixes were prepared by manually mixing 30 g calcium caseinate powder with 70 g demi-water (100% H_2O), 35 g demi-water+38.9 g heavy water (50%v/v H_2O+50%v/v D_2O) or 77.7 g heavy water (100% D_2O). The premixes were transferred to the pre-heated (50°C) shearing device and processed with a rotating speed of 150 rpm for 5 min. After processing, the samples were cooled to 4°C in 10 min before removal from the device. They were stored at −20°C for further analysis. Two sets of samples were made for duplicate measurements.

2.3. Neutron refraction

The effect of the refracted neutron is measured by the SESANS instrument at the neutron source in Delft University of Technology, the Netherlands. The principle of this instrument involves the Larmor precession of a polarised neutron beam in a magnetic field, where the angular deviations of the neutron trajectory due to scattering or refraction are encoded by the measured polarisation P (Bouwman et al., 2004; Rekveldt et al., 2002). When the air bubble is small (e.g., up to a few μm), only elastic scattering contributes to the change in polarisation. However, when the air bubble is large (e.g., over tens of μm), refraction of the neutrons becomes the dominant cause of change in polarisation. The transition from scattering to refraction is continuous. For the cross-over region, we need more advanced theory, such as the phase-object approximation (de Haan et al., 2007a; 2007b), to calculate the angle distribution function. Nevertheless, we can estimate a size limit for this transition. It is calculated by the phase change of the neutron wave function when going through the air and protein interface. When the phase change is of the order of π, refraction becomes dominant (de Haan et al., 2007b). The neutron wave phase change η is calculated as

$$\eta = \left|\frac{4\pi\delta\, R}{\lambda}\right| \tag{1}$$

where R is the radius of a sphere, λ is the wavelength of the neutron, the SESANS instrument in Delft uses thermal neutrons with a wavelength of 2.1±0.1A°, δ is the difference between the neutron refractive index and 1.

$$\delta = \frac{\Delta\text{SLD}\cdot\lambda^2}{2\pi} \tag{2}$$

ΔSLD is the scattering length density contrast between the protein matrix and the air bubbles. For the samples made of 100% D_2O, this number is $5.02 \times 10^{14}\text{m}^{-2}$, for the sample made of 50%v/v H_2O+50%v/v D_2O, $\Delta\text{SLD} = 2.74 \times 10^{14}\text{m}^{-2}$, and ΔSLD equals to $0.208 \times 10^{14}\text{m}^{-2}$ for the sample made of 100% H_2O. Knowing λ and δ, we calculated the minimum air bubble size, and can be sure that refraction dominates the measured signal when the size is around 30μm.

The fibrous protein gels were prepared in their frozen state for optimal sample manipulation. They were cut into approximately $15 \times 12 \times 2.5\text{mm}$ $(L \times H \times W)$ pieces, where the length corresponds to the shear flow direction, the height corresponds to the vorticity direction and the width corresponds to the velocity gradient. Neutrons enter the sample along the velocity gradient with a beam size of $10 \times 8\text{mm}$. We define the direction of the neutron beam as the $x-axis$, and the direction perpendicular to the horizontal plane as the $z-axis$. To see the anisotropy of the air bubbles, the cut gel pieces were first placed with their lengths perpendicular to the $xz-plane$ (Fig. 2B). We denoted this as the horizontal orientation. Afterward, the sample was rotated 90° along the $yz-plane$ and measured with its length parallel to the $z-axis$. This will be further referred to as the vertical orientation.

The sample made of 100% H_2O was measured in this state and after soaking in pure D_2O for 4 h to ensure a complete solvent exchange. Afterward, the sample was sealed in a quartz container filled with D_2O prior to the measurement.

2.4. X-ray tomography (XRT)

The samples were cut into approximately $7 \times 4 \times 3$ mm $(L \times H \times W)$ pieces, where the length corresponds to the shear flow direction, the height corresponds to the vorticity direction and the width corresponds to the velocity gradient. A GE Phoenix v|tomex|m tomographer (General Electric, Wunstorf, Germany) set at 80 kV/90 μA was used to scan the samples. The system contains two X-ray sources. The 240 kV micro focus tube with tungsten target was employed. The images were recorded by a GE DXR detector array with 2024 × 2024 pixels (pixel size 200 μm). The object and detector were located 28.55 mm and 815 mm from the X-ray source. This results in a spatial resolution of 7.00 μm. A full scan consists of 750 projections over 360°. GE reconstruction software (Wunstorf, Germany) was used to calculate the 3D structure via back projection. The 3D images were analyzed using Avizo imaging software version 9.3.0. The area and volume fraction, average width as well as deformation degree (*DoD*) of the air bubbles were calculated from the program. *DoD* is defined as the average of DoD_x and DoD_z, where

$$DoD_x = \frac{y-x}{y+x}$$

$$DoD_z = \frac{y-z}{y+z}$$

$$DoD = \frac{DoD_x + DoD_y}{2}$$

Here, y is the length of a deformed air bubble parallel to the shear flow direction, x is the width of the air bubble parallel to the velocity gradient, and z is the height of the air bubble parallel to the vorticity direction. An illustration can be found in Fig. 2B.

2.5. Refractive light microscope

The samples were imaged using a Digital Microscope (Keyence VHX-2000E) with a magnification of × 100 times.

3. The refraction model

The refraction model is built based on the observation from the refractive microscopy pictures in Fig. 1. These show that the air bubbles are prolate spheroid-like. Hence we approximate the bubble as a spherocylinder which is a cylinder with spherical end caps. We could also do the analysis with elliptical shapes, where we expect similar descriptions of the signals, but the calculation with the spherocylinder is easier. The cross-section of the cylinder parallel to the neutron beam is assumed to be circular (which means the cylinder is perpendicular to the beam). This circular cross-section is confirmed by microscopy picture and 2D x-ray radiography, as presented in the supplementary information.

We present the expected polarisation due to the refraction of the air bubbles as equation (3), with a schematic illustration in Fig. 2. Suppose the protein slab is composed of n layers. Within each layer, the projected area fraction of the air bubbles is defined as α, so $1-\alpha$ represents the fraction of the non-refracting protein gel. The area fraction of the cylinder is defined as β in equation (4), so $\alpha \cdot \beta \cdot P_{cylinder}$ represents the effect of refraction on the polarisation from the cylinders, and $\alpha \cdot (1-\beta) \cdot P_{sphere}$ represents the refraction from the spherical end caps. The total refraction equals to the product of n layers.

$$P_{air\ bubbles} \approx P_{Spherocylinder} = \left[1 - \alpha + \alpha \cdot \beta \cdot P_{cylinder} + \alpha \cdot (1-\beta) \cdot P_{sphere}\right]^n \tag{3}$$

$$\beta = \frac{A_{cylinder}}{A_{cylinder} + A_{spheres}} = \frac{2l}{2l + \pi R} \tag{4}$$

The effect of refraction of the cylinder on the polarisation can be calculated (Plomp et al., 2007) as:

$$P_{cylinder}(B, \gamma) = \kappa(\gamma) \cdot K_1[\kappa(\gamma)] \tag{5}$$

where K_1 is the first-order modified Bessel function of the second kind and

$$\kappa = 4\delta \cdot cos(\gamma) \cdot c \cdot L \cdot cot\theta_0 \cdot B \cdot \lambda \tag{6}$$

in which B represents the magnetic field, the independent variable when using a monochromatic beam; $c = 4.632 \cdot 10^{14} \text{T}^{-1}\text{m}^{-2}$, which is the Larmor precession constant; $L = 1.31$ m, it is the length between the third and fourth magnets and $\theta_0 = 5.5°$, is the inclination angle of the π flipper in the SESANS instrument; γ is the angle between the axis of the cylinder and the $y-axis$ in the $yz-$-$plane$, depicted in Fig. 3. $cos(\gamma)$ takes care of the slit smearing due to the rotation of the cylinder. As the SESANS instrument in Delft is sensitive to refraction in the $z-direction$, the change in polarisation will be the largest when the axis of the cylinder is placed parallel to the $y-axis$, i.e $\gamma = 0°$. Conversely, when it is placed parallel to the $z-axis$, i.e $\gamma = 90°$, no change in polarisation is expected.

The refraction of the sphere can be calculated from the cylinder by numerically integrating γ over 2π:

$$P_{sphere}(B) = \frac{1}{2\pi} \int_0^{2\pi} P_{cylinder}(B, \gamma) d\gamma \tag{7}$$

An illustration can be found in Fig. 3. When the neutron enters

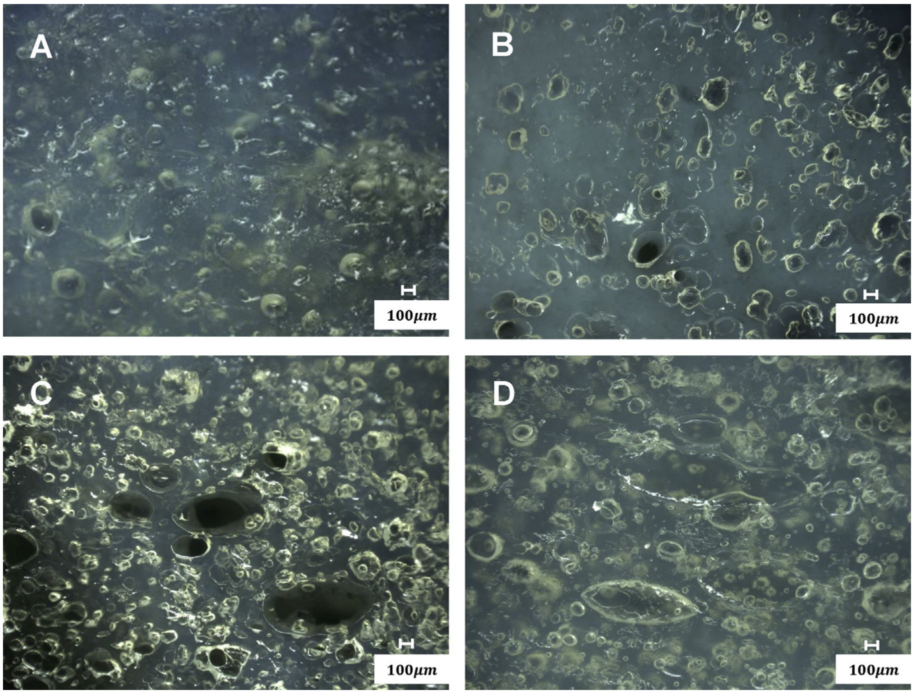

Fig. 1. Optical microscopy pictures of samples made of A: 100% H_2O, B: 100% H_2O after the solvent exchange with D_2O, C: 50%v/v H_2O+50%v/v D_2O, D: 100% D_2O.

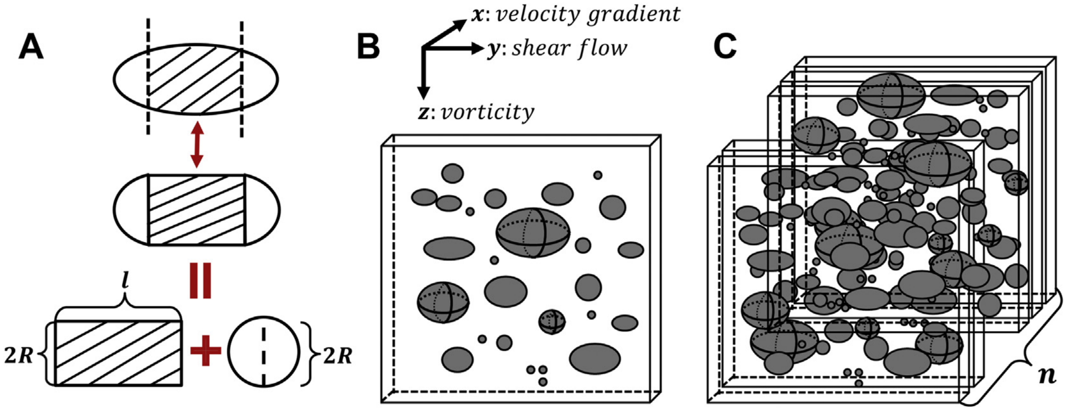

Fig. 2. A: A projection of the air bubbles onto the *zy−plane*. It is approximated by a cylinder with spherical end caps, which equals to the sum of the refraction from a cylinder and a sphere. B: A schematic drawing of one layer of the sample, with the coordinate axis on top. The neutron enters along the *x−axis*. The grey prolate spheroid-like particles represent the air bubbles. C: The total refraction is contributed by n layers stacked together.

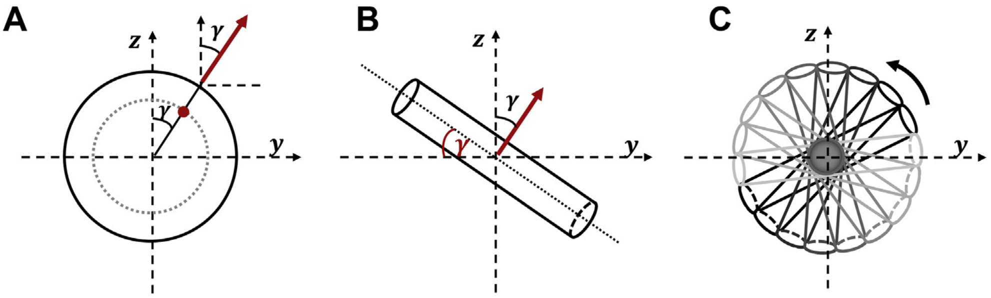

Fig. 3. Schematic drawings compare the refraction of a sphere to the refraction of a cylinder. A: the neutron (red dot) enters a sphere with an angle of γ. B: the neutron enters a cylinder with its axis tilted with γ. C: The refraction of a sphere (grey circle) equals to the axially averaged refraction of a cylinder. (For interpretation of the references to colour in this figure legend, the reader is referred to the Web version of this article.)

the sphere with an angle of γ (dot in Fig. 3A), its refraction is equivalent to a cylinder with its axis tilted with γ (Fig. 3B). Rotating this cylinder over 360° (Fig. 3C), the averaged total refraction of the cylinder equals to the refraction of a sphere. To validate the refraction of a sphere, we applied the model to some glass microspheres that can be find in the supplementary information.

A comparison between equations (5) and (7) reveals that the refraction of the cylinder is dependent on the angular orientation, while not for the sphere. This means if we measure the sample horizontally and vertically, equation (3) will be specified into two:

$$P_{hor}(B) = \left[1 - \alpha + \alpha \cdot \beta \cdot P_{cylinder}(B) + \alpha \cdot (1-\beta) \cdot P_{sphere}(B)\right]^n \tag{8}$$

and

$$P_{ver}(B) = \left[1 - \alpha + \alpha \cdot \beta + \alpha \cdot (1-\beta) \cdot P_{sphere}(B)\right]^n \tag{9}$$

Equations (8) and (9) will use the same α, β and n to fit the horizontal and vertical orientation of the sample.

4. Results

4.1. Neutron refraction

Two sets of calcium caseinate (CaCas) fibrous gels were measured. Each set contains three samples made of 100% H_2O, 50%v/v H_2O+50%v/v D_2O (this sample will be further referred to as 50% D_2O) and 100% D_2O. Since the model is sensitive to the orientation and shape of the air bubbles, each sample was measured in two directions: horizontally (shear flow direction being parallel to the $y-axis$) and vertically (shear flow direction being parallel to the $z-axis$). Equations (8) and (9) were used to fit the data.

Fig. 4 shows the results of one set of samples. The depolarisation is measured as a function of magnetic field. The duplicate samples give a similar result. The 100% H_2O sample measured ex-situ (hollow symbol in Fig. 4A) gives no signal, probably due to the low contrast. To increase the contrast, we put the sample in a quartz cell filled with pure D_2O and measured it again. The estimated new contrast is $\approx 5.7 \times 10^{14} \mathrm{m}^{-2}$, taking into account 10% of the hydrogen in the sample exchange with deuterium in D_2O. A clear signal can be obtained this way (filled symbol in Fig. 4A).

For all three samples, the horizontal orientation depolarises more than the vertical orientation. As mentioned, the instrument in

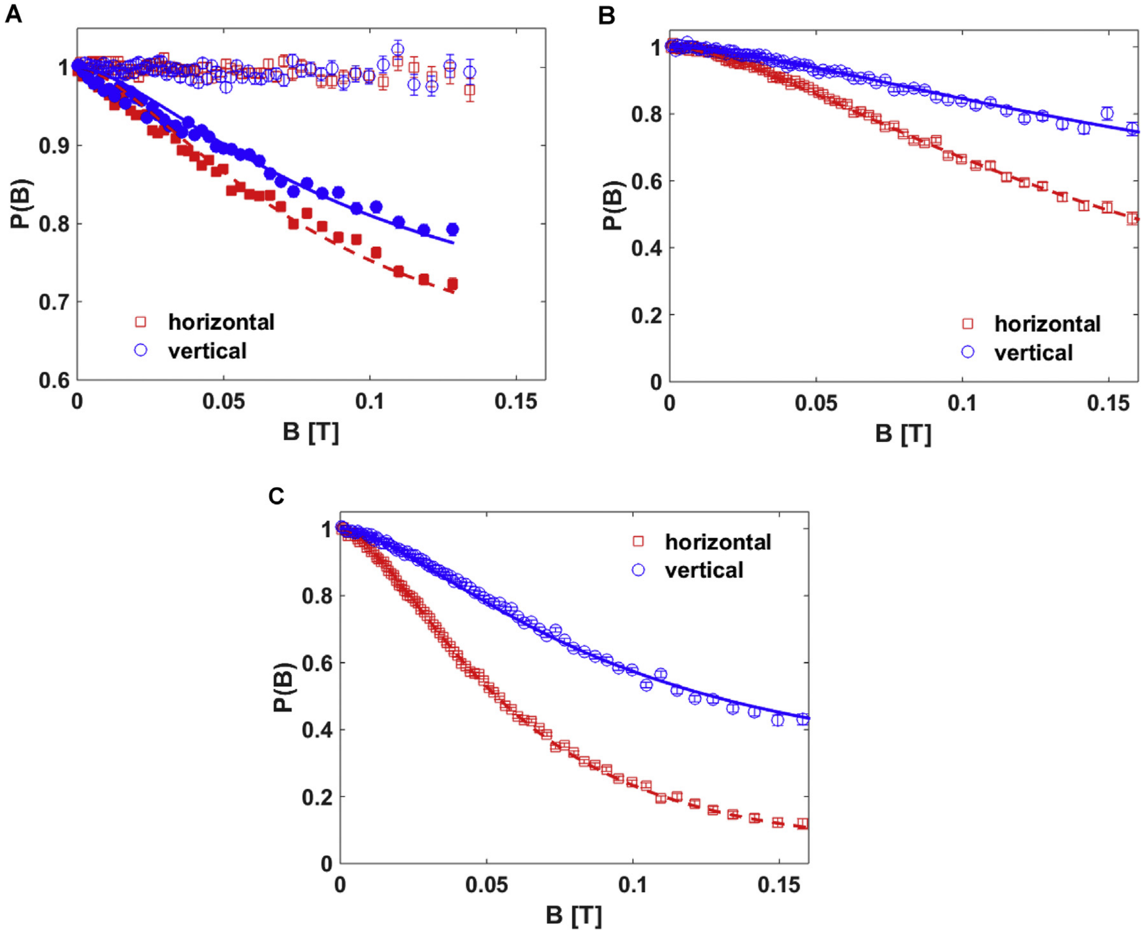

Fig. 4. Polarisation as a function of applied magnetic field. A: CaCas made of 100% H_2O; B: CaCas made of 50% D_2O; C: CaCas made of 100% D_2O. The square symbols represents the horizontal orientation of the sample, and the circles represents the vertical orientation. The hollow symbols are sample measured ex-situ whilst the filled symbols are measured with the sample sealed in D_2O. Lines are the fitted results using the refraction model.

Delft is sensitive to the $z-axis$, meaning that the air bubbles are elongated in the shear flow direction ($y-axis$). The difference in depolarisation between the horizontal and vertical orientation is the largest in the sample made of 100% D_2O, indicating the air bubbles in this sample are elongated to a higher extent than the others. Furthermore, the 100% D_2O sample contained more air bubbles than the 100% H_2O one, given the fact that after the solvent exchange, the sample made of 100% H_2O depolarised less than the 100% D_2O one, despite a similar contrast. This finding is supported by Fig. 1, where the air bubbles in the 100% H_2O samples (Fig. 1A) are less elongated and somewhat smaller than the other two (Fig. 1C&D). Fig. 1B is the 100% H_2O sample after the solvent exchange. It shows that the shape and size of the air bubbles remained intact, suggesting that solvent exchange has little impact on their morphologies.

The first three rows in Table 1 show the area fraction of the air bubbles in one layer α, the number of layers n and area fraction of the cylinder β fitted from the refraction model. The standard deviation of the 100% H_2O sample is very large. It appears α and n are highly correlated for this particular sample. It could be due to an inaccurate estimation of the contrast since only this sample was soaked in D_2O.

Looking at the 50% and 100% D_2O samples, the fitted results of α and n vary considerably between duplicates. However, this does not mean the model is unconvincing, since the standard deviation of each parameter remained small. As a result, we owe the large variation to the heterogeneous character of the sample itself.

Though α and n can describe the effect of refraction very well, they don't necessarily contain any direct size information of the sample. Fortunately, the product of α and n contains such information. It is because size information such as dimension and shape is reflected in the total area fraction ($=\alpha \times n$) instead of area fraction in one layer, which means they are convolved in the product of α and n. Thus we need to rewrite $\alpha \times n$ into other expressions in order to derive the dimension and shape of the air bubbles.

Based on its definition, $\alpha \times n$ is expressed as:

$$\alpha \times n = \frac{\left(\pi R^2 + 2Rl\right) \cdot N}{A_s} \tag{10}$$

Where $\pi R^2 + 2Rl$ is the cross-section area of one spherocylinder, N is the total number of spherocylinders in the sample, A_s is the area of the sample covered by the neutron beam. A_s can be expressed as the volume V_s of the sample divided by its thickness t: $A_s = V_s/t$. V_s can be expressed into the total volume of the spherocylinder divided by its volume fraction ϕ:

$$V_s = \frac{\left(\frac{4}{3}\pi R^3 + \pi R^2 l\right) \cdot N}{\phi} \tag{11}$$

Where $\frac{4}{3}\pi R^3 + \pi R^2 l$ is the volume of one spherocylinder. Inserting equation (11) into equation (10) yields:

$$\alpha \times n = \frac{\phi \cdot t \cdot (\pi R + 2l)}{\frac{4}{3}\pi R^2 + \pi R l} \tag{12}$$

Substituting l with β and R using equation (4) yields:

$$\alpha \times n = \frac{\phi \cdot t}{R} \cdot \frac{1}{\frac{4}{3}(1-\beta) + \frac{\pi}{2} \cdot \beta} \tag{13}$$

Equation (13) shows that the product of α and n is related to the volume fraction ϕ of the air bubbles, thickness t, area fraction of the cylinder β and radius of the sphere R. Given ϕ and t are measurable and $\alpha \times n$ and β can be fitted, we can extract a size parameter R from the above equation. As for β, equation (4) shows that β is essentially related to the dimensions of the spherocylinder. We rewrite this parameter into the earlier defined 'Degree of Deformation' (DoD) so that it becomes comparable to the XRT data in section 4.2. $DoD = \frac{l}{l+4R} = \frac{\pi}{\pi + 8\left(\frac{1}{\beta} - 1\right)}$. A larger DoD means the air bubbles are more elongated. $\alpha \times n$, 2R and DoD can be found in Table 1.

From the fitted parameters, we learned that the average width (2R) of the air bubbles in the 100% D_2O sample is almost the same as the 50% D_2O. Both are much larger than the 100% H_2O sample. The bubbles in the 100% D_2O and the 50% D_2O samples are also deformed to a similar extent, suggesting that they are more affected by the shear flow. Whereas for the 100% H_2O sample, the *DoD* index is quite small, suggesting the air bubbles mostly remained spherical.

Our initial assumption when preparing the samples with different H_2O to D_2O ratios was that the only difference between them is the contrast. The fitted results suggest otherwise. It seems that D_2O had an unexpected influence on the size and shape of the air bubbles in the final structure. In the next section, we will present XRT data to support these findings.

4.2. X-ray tomography

In neutron refraction, the parameters 2R and *DoD* are an average representation of all the air bubbles in the sample. With XRT, the 2R and *DoD* of every single air bubble can be obtained. We first present the 3D reconstructed tomography of the three samples in Fig. 5. It is clear that the sample made of 100% H_2O contains fewer air bubbles than the other two. The air bubbles are also smaller, which corresponds to the fitted width (2R) of the spherocylinder. Next, we present the distributions of the number of air bubbles (*Number*) and the degree of deformation (*DoD*) based on the cross-section area. The cross-section area is defined as $\frac{\pi}{4} \cdot a \cdot b$, where a and b is the length of the long and short axes of an ellipsoid. The results are shown in Table 2.

Similar to the neutron refraction data, the differences between the two sets of samples are large, suggesting inhomogeneities in

Table 1
α, n and β are fitted from the refraction model, ϕ from the XRT data. *DoD* and 2R are calculated using $\alpha \times n$, β and ϕ. The errorbars are the standard deviations calculated using the Bootstrap methods (Efron, 1992). The 100% H_2O sample substituted with D_2O was measured only once.

	100% H_2O	50% D_2O−1	50% D_2O−2	100% D_2O−1	100% D_2O−2
α	0.014±0.009	0.87 ± 0.07	0.38 ± 0.04	0.74 ± 0.02	0.79 ± 0.02
n	40.0 ± 13.8	1.4 ± 0.1	3.9 ± 0.4	3.1 ± 0.1	1.6 ± 0.1
β	0.184 ± 0.003	0.414 ± 0.008	0.437 ± 0.006	0.447 ± 0.002	0.476 ± 0.002
ϕ	0.023	0.142	0.160	0.154	0.122
$\alpha \times n$	0.560 ± 0.002	1.25 ± 0.01	1.48 ± 0.01	2.23 ± 0.01	1.29 ± 0.01
2R (μm)	147 ± 1	332 ± 3	302 ± 1	239 ± 1	390 ± 2
DoD	0.081 ± 0.002	0.217 ± 0.006	0.233 ± 0.004	0.241 ± 0.002	0.263 ± 0.001

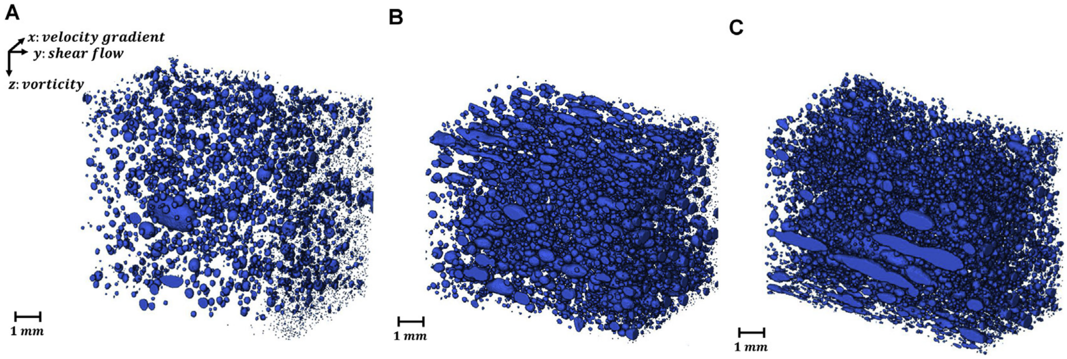

Fig. 5. 3D reconstructed tomography of one set of the samples. The samples are made of A: 100% H_2O; B: 50% D_2O and C: 100% D_2O.

Table 2
XRT results: the distribution of the *Number* of bubbles per volume and the *DoD* calculated based on the cross-section area. The values are an average of two measurements, the errorbars are differences from the mean.

	cross-section area (mm^2)	100% H_2O	50% D_2O	100% D_2O
Number	≤0.01	11103 ± 5495	5900 ± 945	8116 ± 1648
	0.01~0.1	1287 ± 33	2326 ± 41	3012 ± 13
	0.1~1	31 ± 2	201 ± 18	211 ± 46
	≥1	1 ± 0	8 ± 3	6 ± 1
DoD	≤0.01	−0.067 ± 0.021	−0.009 ± 0.002	−0.001 ± 0.002
	0.01~0.1	−0.019 ± 0.019	0.063 ± 0.016	0.058 ± 0.019
	0.1~1	−0.015 ± 0.007	0.207 ± 0.000	0.210 ± 0.076
	≥1	0.338 ± 0.011	0.522 ± 0.035	0.417 ± 0.090

the samples. For all three samples, the number of air bubbles decreased with increasing cross-section area, while the *DoD* increased with increasing cross-section area. The few large air bubbles are more susceptible to shear than the smaller ones. Further, both parameters are much larger when D_2O is present in the system. D_2O seemed to be responsible for larger air bubbles sizes and higher extent of elongation.

Since the *Numbers*, sizes and *DoD* affect the air bubble area and volume simultaneously, we plotted the average area, volume and their fractions in Figs. 6 and 7. For comparison, we also included the calculated average area and volume in the figure using the fitted results from the refraction data. The average area and volume of the spherocylinder are calculated as $\pi R^2 + 2Rl$ and $\frac{4}{3}\pi R^3 + \pi R^2 l$ respectively. In Fig. 6 left, the calculated average area of the air bubble from the refraction model in the 100% H_2O sample corresponds well to the cross-section area between 0.01~0.1 mm^2. This cross-section area happens to take up the largest area fraction (Fig. 6 right). Similarly, the average area of the 50% and 100% D_2O samples fall in between 0.01~1 mm^2, the sum of the two area fractions takes up around 75%. This trend applies to volume fraction as well. Fig. 7 shows that the calculated average volume of the air bubble falls into the cross-section area who takes up the largest volume fraction for all the samples. To summarise, the fitted parameters from the refraction model are representative of the air bubbles that take up the largest area and volume.

5. Discussion

"Foods are a complex and heterogeneous system." (Donald, 2004), because of this, we utilized several techniques to ensure an objective and thorough understanding of the system. The refractive microscope provides valuable, descriptive information of the air

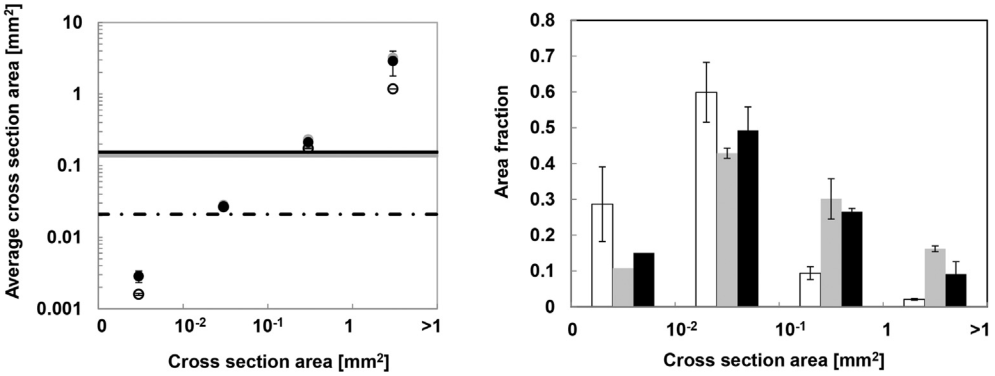

Fig. 6. Left: average cross-section area of the air bubble calculated from the neutron refraction model (lines) versus the cross-section areas from the XRT data (symbols). The 100% H_2O sample is represented by the dash-dot line and hollow circles; the 50% D_2O sample is represented by the grey line and grey circles; The 100% D_2O sample is represented by the black line and black circles; Right: area fraction based on cross-section area. The white, grey and black bars correspond to sample made of 100% H_2O, 50% D_2O and 100% D_2O.

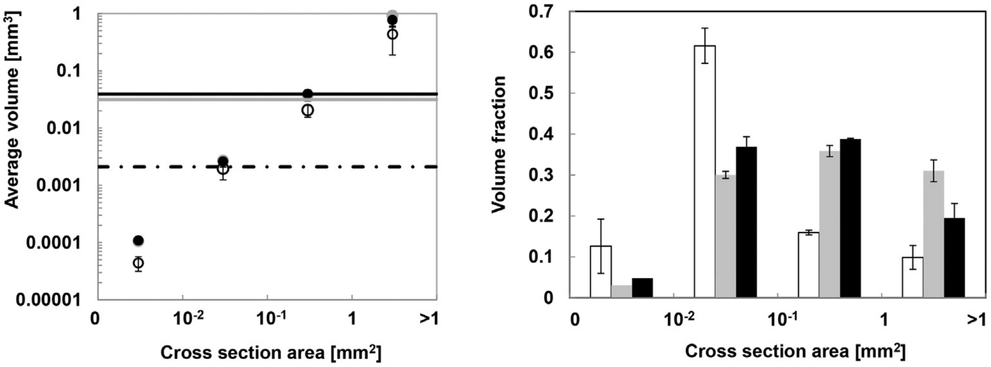

Fig. 7. Left: average volume of the air bubble calculated from the neutron refraction model (lines) versus the volumes from the XRT data (symbols). The 100% H_2O sample is represented by the dash-dot line and hollow circles; the 50% D_2O sample is represented by the grey line and grey circles; The 100% D_2O sample is represented by the black line and black circles; Right: volume fraction based on cross-section area. The white, grey and black bars correspond to sample made of 100% H_2O, 50% D_2O and 100% D_2O.

bubbles. However, the sample volume that can be probed by the microscope is very limited, thus the information may not be representative of the whole system. To quantify the sample with a larger volume, we used two complementary techniques: neutron refraction and XRT. They are compared in the following aspects:

1) Sensitivity to contrast: XRT can distinguish well between the protein matrix and air bubbles without any pretreatment, while the initial contrast for neutron refraction is insufficient. Two methods can be used to increase the neutron refraction contrast. One is solvent exchange after obtaining the sample, the other one is replacing H_2O with D_2O during the production of the sample. In our study, the first method worked better, since it has little perturbation on the structure, as shown by the microscopy image of the 100% H_2O sample after soaking in D_2O. The latter method highlighted the unwanted influence of D_2O on the morphology of the air bubbles, probably because the structure of the protein matrix was changed. It could be that D_2O has a stronger D-D bond than H_2O, which imposes a more hydrophobic environment onto the calcium caseinate. The consequences are delayed wetting of the protein powder, the hydrophobic parts of the protein become more compact and more rigid aggregates (Oakenfull & Scott, 2003). These factors contribute to a more elastic gel network that will be more susceptible to shear (Manski et al., 2007c). In addition, an increase in elasticity is related to a better air entrapping ability. As a result, when applying the neutron refraction technique, the choice of method to increase the contrast depends on the susceptibility of the food building blocks to the solvent environment.
2) Advantages and Drawbacks: For neutron refraction, the advantages are i) objectivity of the method in sense of data processing and interpretation; ii) nnly a few parameters are needed to give a quantitative description of the sample; iii) it can probe a relatively large sample size. The advantages of XRT are i) no pretreatment is needed prior to the measurement; ii) higher accessibility to the instrument and iii) the 2D/3D reconstructed results are straightforward. The drawback of neutron refraction is the potential effect of D_2O on the morphology of the air bubbles. Though we suspect the effect will be negligible in other food materials such as fat or cellulose. For XRT, the drawbacks are the imaging artifacts during image acquisition and operator dependency during image analysis. Both may render the results less reproducible. This is also why we promote utilizing multiple techniques to increase certainty in the interpretation of a complex system.
3) Future prospects: currently, XRT has far more applications in food products compared to neutron refraction. Nevertheless, the neutron refraction technique has the potential to be applied to other composite food materials, as long as there is sufficient contrast between the filler and the matrix, and the filler has a desired size range. For instance, it can be used to study the distribution of fat in different types of sausages (Frisullo, Laverse, Marino, & Del Nobile, 2009), or the stability of aerated food products (Ellis, Norton, Mills, & Norton, 2017).

6. Conclusion

Air bubbles in a composite meat analogue made of calcium caseinate are studied by the neutron refraction technique, XRT and microscope. A model was constructed to calculate the depolarisation of the neutrons refracted by air bubbles in the fibrous protein gels. Average width, deformation direction and degree of the air bubbles can be obtained from the model which agreed well with the XRT data and microscopy image. These parameters represent an average of the system given they correspond to the largest area and volume fraction of the air bubbles in the XRT data. This technique may be a standard routine in future and has the potential to be applied to other composite food systems, as long as structural differences caused by D_2O are taken into account.

Acknowledgment

We would like to thank Dr. Jeroen Plomp for useful discussion on the refraction theory; Dr. Jouke Heringa for data fitting; Chris Duif for assisting the SESANS measurements and Remco Hamoen for conducting the XRT measurements. This work is part of the research programme SSCANFoods, which is partly financed by the Netherlands Organisation for Scientific Research (13386).

Appendix A. Supplementary data

Supplementary data related to this article can be found at https://doi.org/10.1016/j.foodhyd.2018.05.006.

References

van Dalen, G., Blonk, H., van Aalst, H., & Hendriks, C. L. (2003). 3-d imaging of foods using x-ray microtomography. *GIT Imaging and Microscopy, 3*, 18–21.
van der Sman, R. (2016). Filler functionality in edible solid foams. *Advances in Colloid and Interface Science, 231*, 23–35.
van der Zalm, E., Berghout, J., van der Goot, A., & Boom, R. (2012). Starch–gluten

separation by shearing: Influence of the device geometry. *Chemical Engineering Science, 73*, 421–430.

Afoakwa, E. O., Paterson, A., & Fowler, M. (2007). Factors influencing rheological and textural qualities in chocolate–a review. *Trends in Food Science & Technology, 18*(6), 290–298.

van Aken, G. A., Oliver, L., & Scholten, E. (2015). Rheological effect of particle clustering in gelled dispersions. *Food Hydrocolloids, 48*, 102–109.

Bellido, G. G., Scanlon, M. G., Page, J. H., & Hallgrimsson, B. (2006). The bubble size distribution in wheat flour dough. *Food Research International, 39*(10), 1058–1066.

Berk, N., & Hardman-Rhyne, K. (1988). Analysis of sas data dominated by multiple scattering. *Journal of Applied Crystallography, 21*(6), 645–651.

Bouwman, W. G., Krouglov, T. V., Plomp, J., Grigoriev, S. V., Kraan, W. H., & Rekveldt, M. T. (2004). Sesans studies of colloid phase transitions, dairy products and polymer fibres. *Physica B: Condensed Matter, 350*(1), 140–146.

Bryant, A., Ustunol, Z., & Steffe, J. (1995). Texture of cheddar cheese as influenced by fat reduction. *Journal of Food Science, 60*(6), 1216–1219.

Cnudde, V., & Boone, M. N. (2013). High-resolution x-ray computed tomography in geosciences: A review of the current technology and applications. *Earth-science Reviews, 123*, 1–17.

Das, S., Maroli, A., Singh, S. S., Stannard, T., Xiao, X., Chawla, N., et al. (2016). A microstructure-guided constitutive modeling approach for random heterogeneous materials: Application to structural binders. *Computational Materials Science, 119*, 52–64.

Dekkers, B. L., Hamoen, R., Boom, R. M., & van der Goot, A. J. (2018). Understanding fiber formation in a concentrated soy protein isolate-pectin blend. *Journal of Food Engineering, 222*, 84–92.

Demirkesen, I., Kelkar, S., Campanella, O. H., Sumnu, G., Sahin, S., & Okos, M. (2014). Characterization of structure of gluten-free breads by using x-ray microtomography. *Food Hydrocolloids, 36*, 37–44.

Dobraszczyk, B., & Morgenstern, M. (2003). Rheology and the breadmaking process. *Journal of Cereal Science, 38*(3), 229–245.

Donald, A. (2004). Food for thought. *Nature Materials, 3*, 579–581.

Duquenne, B., Vergauwen, B., Capdepon, C., Boone, M. A., De Schryver, T., Van Hoorebeke, L., et al. (2016). Stabilising frozen dairy mousses by low molecular weight gelatin peptides. *Food Hydrocolloids, 60*, 317–323.

Efron, B. (1992). Bootstrap methods: Another look at the jackknife. In *Breakthroughs in statistics* (pp. 569–593). Springer.

Ellis, A., Norton, A., Mills, T., & Norton, I. (2017). Stabilisation of foams by agar gel particles. *Food Hydrocolloids, 73*, 222–228.

Ersch, C., Meinders, M. B., Bouwman, W. G., Nieuwland, M., van der Linden, E., Venema, P., et al. (2016). Microstructure and rheology of globular protein gels in the presence of gelatin. *Food Hydrocolloids, 55*, 34–46.

Frisullo, P., Laverse, J., Marino, R., & Del Nobile, M. (2009). X-ray computed tomography to study processed meat microstructure. *Journal of Food Engineering, 94*(3), 283–289.

Grabowska, K. J., van der Goot, A. J., & Boom, R. M. (2012). Salt-modulated structure formation in a dense calcium caseinate system. *Food Hydrocolloids, 29*(1), 42–47.

Guo, J., Jin, Y.-C., Yang, X.-Q., Yu, S.-J., Yin, S.-W., & Qi, J.-R. (2013). Computed microtomography and mechanical property analysis of soy protein porous hydrogel prepared by homogenizing and microbial transglutaminase cross-linking. *Food Hydrocolloids, 31*(2), 220–226.

de Haan, V.-O., Plomp, J., Bouwman, W. G., Trinker, M., Rekveldt, M. T., Duif, C. P., et al. (2007). Phase-object approximation in small-angle neutron scattering experiments on silicon gratings. *Journal of Applied Crystallography, 40*(1), 151–157.

de Haan, V.-O., Plomp, J., & van Well, A. A. (2007). Real-space form factor of spherical particles in kinematic and dynamic scattering. *Journal of Applied Crystallography, 40*(4), 756–760.

Krintiras, G. A., Diaz, J. G., Van der Goot, A. J., Stankiewicz, A. I., & Stefanidis, G. D. (2016). On the use of the Couette cell technology for large scale production of textured soy-based meat replacers. *Journal of Food Engineering, 169*, 205–213.

Krintiras, G. A., Göbel, J., Bouwman, W. G., Van Der Goot, A. J., & Stefanidis, G. D. (2014). On characterization of anisotropic plant protein structures. *Food & function, 5*(12), 3233–3240.

Kuang, X., Ying, G., Ranieri, V., & Sansalone, J. (2015). Examination of pervious pavement pore parameters with x-ray tomography. *Journal of Environmental Engineering, 141*(10), 04015021.

Maire, E., & Withers, P. J. (2014). Quantitative x-ray tomography. *International Materials Reviews, 59*(1), 1–43.

Manski, J. M., van der Goot, A. J., & Boom, R. M. (2007). Formation of fibrous materials from dense calcium caseinate dispersions. *Biomacromolecules, 8*(4), 1271–1279.

Manski, J. M., van der Goot, A. J., & Boom, R. M. (2007b). Advances in structure formation of anisotropic protein-rich foods through novel processing concepts. *Trends in Food Science & Technology, 18*(11), 546–557.

Manski, J. M., van Riemsdijk, L. E., van der Goot, A. J., & Boom, R. M. (2007). Importance of intrinsic properties of dense caseinate dispersions for structure formation. *Biomacromolecules, 8*(11), 3540–3547.

Nieuwland, M., Bouwman, W. G., Bennink, M. L., Silletti, E., & de Jongh, H. H. (2015). Characterizing length scales that determine the mechanical behavior of gels from crosslinked casein micelles. *Food Biophysics, 10*(4), 416–427.

Oakenfull, D., & Scott, A. (2003). Gelatin gels in deuterium oxide. *Food Hydrocolloids, 17*(2), 207–210.

Plomp, J., Barker, J., De Haan, V., Bouwman, W., & van Well, A. (2007). Neutron refraction by cylindrical metal wires. *Nuclear Instruments and Methods in Physics Research Section a: Accelerators, Spectrometers, Detectors and Associated Equipment, 574*(2), 324–329.

Rekveldt, M. T., Bouwman, W., Kraan, W., Uca, O., Grigoriev, S., Habicht, K., et al. (2002). Elastic neutron scattering measurements using larmor precession of polarized neutrons. In *Neutron Spin echo spectroscopy* (pp. 87–99). Springer.

Schoeman, L., Williams, P., du Plessis, A., & Manley, M. (2016). X-ray micro-computed tomography (μct) for non-destructive characterisation of food microstructure. *Trends in Food Science & Technology, 47*, 10–24.

Tromp, R. H., & Bouwman, W. G. (2007). A novel application of neutron scattering on dairy products. *Food Hydrocolloids, 21*(2), 154–158.